Soft Matter

Dynamic Article Links

Cite this: *Soft Matter*, 2011, **7**, 9276

www.rsc.org/softmatter

PAPER

Surface and interface porosity of polymer/fullerene-derivative thin films revealed by contrast variation of neutron and X-ray reflectivity†

Heng-Jui Liu,[ab] U-Ser Jeng,*[a] Norifumi L. Yamada,[c] An-Chung Su,[d] Wei-Ru Wu,[a] Chun-Jen Su,[a] Su-Jien Lin,[b] Kung-Hwa Wei[e] and Mao-Yuan Chiu[e]

Received 30th May 2011, Accepted 25th July 2011
DOI: 10.1039/c1sm06005h

Contrast variation of neutron and X-ray reflections has been adapted to reveal the film in-depth (vertical) composition profiles of the blend of poly(3-hexylthiophene) (P3HT) and [6,6]-phenyl-C61-butyric acid methyl ester (PCBM) for bulk heterojunction thin-film solar cells, with a PCBM/P3HT weight ratio of $c = 0.6$, 0.8 and 1.0. The X-ray scattering-length-density (SLD) profiles, extracted from X-ray reflectivity for the blend films spun-cast on Si wafer, exhibit a stratified film morphology of *ca.* 85 nm film thickness; the corresponding neutron SLD profiles extracted for the same films further elucidate a PCBM-enriched interfacial layer adjacent to the Si substrate. In contrast to the often assumed two-phase model, a three-phase model with porosity included as the third phase has to be used in deducing the absolute volume fractions of PCBM and P3HT from the complementary neutron and X-ray SLD profiles. In general, the thus deduced in-depth composition profiles for the blend films comprise a substantial surface layer (10–15 nm) of *ca.* 40% porosity, a 50 nm main layer with relatively uniform PCBM–P3HT composition, and a PCBM-enriched interface layer (~20 nm) with ~15% porosity. Formation of the surface porosity is related to interfacial instability occurred in a transient surface layer upon film drying. Annealing at 150 °C influences modestly the vertical phase separation of the film, but drastically activates local phase separation for formation and growth of PCBM and P3HT nanodomains, as revealed by grazing incidence small/wide angle X-ray scattering. The surface/interface porosity features (overlooked in nearly all the previous studies) and the composition-dependent vertical phase separation bear hints in advancing device performance *via* interfacial morphology optimization.

1. Introduction

Manipulating the nanostructure of the active layer of bulk heterojunction (BHJ) thin-film solar cells plays one of the primary factors in improving device performance.[1,2] Accumulated experimental evidence from microscopic techniques have shown that an optimized structure of the BHJ thin-film solar cells, such as the efficient blend of poly(3-hexylthiophene) (P3HT) and [6,6]-phenyl-C61-butyric acid methyl ester (PCBM), features in phase-separated nanodomains of abundant interfaces to account for both the efficiencies of dissociation and diffusion of excitons.[3,4] Complementary to imaging studies, grazing incidence X-ray diffraction indicated that the lamellar domains of P3HT stacked mainly along the film surface in the normal direction of the spin-cast P3HT/PCBM thin films.[5–7] In addition, grazing incidence small-angle X-ray scattering (GISAXS) or small-angle neutron scattering captured quick formation of PCBM nano-aggregates in the P3HT matrix upon annealing.[8–12] In our previous study,[12] the nanodomain structures and formation mechanisms of PCBM aggregates and P3HT crystallites of the P3HT/PCBM blend upon annealing were elucidated respectively to be diffusion-controlled and constant-nucleation dominated, based on time-resolved, simultaneous grazing-incidence small/wide-angle X-ray scattering (GISAXS/GIWAXS); the fast development of the nanodomains in the active layer of the P3HT/PCBM thin-film solar cells upon short term annealing demonstrated their sensitive influences on the charge mobility, hence, power conversion efficiency.[8,12,13]

Recently, the morphological study with complementary techniques for the phase separation behavior of P3HT and PCBM in the film in-depth (vertical) direction became very active, in an attempt to correlate and utilize the vertical phase separation features of the two components to further improve the device performance.[14] Among the studies, PCBM was found to be

[a]*National Synchrotron Radiation Research Center, 101 Hsin-Ann Road, Hsinchu Science Park, Hsinchu, 30076, Taiwan; Fax: +886-3-578-3813; Tel: +886-3-578-0281*
[b]*Department of Materials Science and Engineering, National Tsing Hua University, Hsinchu, 30013, Taiwan*
[c]*Neutron Science Laboratory, High Energy Accelerator Research Organization, Tokai, Naka, 319-1106, Japan*
[d]*Department of Chemical Engineering, National Tsing Hua University, Hsinchu, 30013, Taiwan*
[e]*Department of Materials Science and Engineering, National Chiao Tung University, Hsinchu, 30050, Taiwan*
† Electronic supplementary information (ESI) available. See DOI: 10.1039/c1sm06005h

This journal is © The Royal Society of Chemistry 2011

enriched near the film–substrate interface of the P3HT/PCBM blend using X-ray photoelectron spectroscopy;[15] with better in-depth spatial resolution, neutron reflectivity revealed a stratified morphology comprised of a main layer of uniform P3HT/PCBM composition and a PCBM-enriched interfacial layer (s).[16,17] Nevertheless, results from variable-angle spectroscopic ellipsometry (VASE) suggested a linearly decreased PCBM concentration starting from the film–substrate interface of the P3HT/PCBM bend film.[18] In contrast, P3HT was observed to be substantially depleted from the film surface according to electron tomography observation, suggesting that the film surface might be PCBM-enriched.[19] However, concentration fluctuations of P3HT initiating from the surface of pure P3HT towards the bulk of the P3HT/PCBM blend were reported based on secondary ion mass spectrometry;[20] consequently, surface-directed spinodal decomposition during solvent evaporation was proposed as a possible mechanism for the vertical and the subsequent lateral (or local) phase separations for bicontinuous P3HT and PCBM nanodomains. Spinodal decomposition, nevertheless, could not account for the phase separation behaviors observed in several other different occasions of the blend.[8,12,21]

In most of the cases mentioned, enrichment of PCBM adjacent to the film–substrate interface was observed for the P3HT/PCBM films similarly processed; however, conclusions on the surface compositions of the films were not aligned. Precise vertical phase separation behavior of this intensively studied system still awaits further scrutiny.[14] We note that in all mentioned studies, the two-phase model, namely, the film space is filled with either P3HT or PCBM, was postulated in the deductions or interpretations of the vertical phase separation of the two components in the films. The vertical composition profile deduced based on selective sensitivity of the employed tools to merely P3HT or PCBM, however, would not be appropriate when the two-phase assumption likely fails near the asymmetric film interface with air or substrate.

This study aims to resolve quantitatively and systematically the vertical composition profiles of the P3HT/PCBM thin films spun-cast on Si wafers, using contrast variation of X-ray and neutron reflectivity (XR/NR) with high spatial resolution in the in-depth direction and excellent film penetration power.[22] We show that a three-phase model with porosity included as the third phase is indispensable to resolve the absolute vertical volume fraction profiles of PCBM and P3HT in the film, especially near the surface and interface. In general, the stratified film morphology observed comprises a surface layer of high porosity, a main layer of uniform composition (being close to the prescribed composition, when below the miscibility limit), and a PCBM-enriched (or P3HT-depleted) interface layer of a small fraction of porosity adjacent to the substrate. The porosity features of the surface and interface transition layers of the two-component system were overlooked in previous abundant studies (with microscopic techniques or scattering tools without contrast variation or adequate spatial resolution). The high surface porosity together with the absolute vertical volume fraction profiles obtained help to reconcile several previously seemingly opposite suggestions on the vertical phase separation behavior of P3HT and PCBM in the blend.[15–19] Also discussed in this study are the mechanistic origins respectively for the 1D vertical phase separation for the stratified morphology upon film drying and the subsequent local phase separation for formation and growth of (3D) PCBM nanograins and P3HT lamellae upon annealing, as revealed by GISAXS/GIWAXS. The present results bear hints in further advancing device performance *via* minimizing porosity for improved interfacial contacts of the active layer with the electrodes of the BHJ thin-film solar cells.

2. Materials and methods

Regioregular (>90%) P3HT (M_w = 50 kDa; 4002-E, Rieke Metals) and PCBM (Nano-C, Inc.) were respectively dissolved in chlorobenzene (CB), 15 mg mL^{-1} each. The two solutions were mixed in different ratios of 1 : 1, 1 : 0.8, and 1 : 0.6 (P3HT : PCBM), and stirred in a glovebox at 65 °C for more than 12 hours. These mixtures were respectively spun-cast (600 rpm, 60 s) onto Si wafers of dimensions of 20 mm by 20 mm, and dried subsequently at ambient temperatures under N_2 gas flow. Prior to spin-coating, the Si wafers were cleaned in detergent then in acetone solutions with ultrasonic treatment, followed by UV-ozone cleaning for 20 min after wafers dried under N_2 flow. Samples were selectively annealed at 150 °C for 15 min in a glovebox under N_2 gas flow. The PCBM volume fractions for thus obtained sample thin films were 30%, 37%, and 42%, respectively.

X-Ray reflectivity data were collected for the sample thin films using either a synchrotron 10 keV ($\lambda = 1.24$ Å) beam of the 17B beamline of the National Synchrotron Radiation Research Center (NSRRC), Taiwan,[23] or an in-house X-ray reflectometer with the wavelength $\lambda = 1.54$ Å. With the BL16 SOFIA neutron reflectometer in J-PARC/MLF, Japan,[24] neutron reflectivity data were collected for the same sample films used in X-ray reflectivity measurements. With the neutron spectrum covering λ from 2.0 to 8.8 Å and three incident angles of $\theta = 0.30°$, 0.8°, and 1.8°, neutron reflectivity (NR) data, collected based on a time-of-flight mode, covered a q_z-range of 0.007–0.15 $Å^{-1}$. The scattering wavevector transfer perpendicular to the sample surface q_z is defined by $4\pi\lambda^{-1}\sin\theta$.

Data analysis

XR or NR data of the P3HT/PCBM films were analyzed using the Parratt32 software package for a best-fitted model profile of in-depth scattering-length-density (SLD).[25] Furthermore, the thus obtained mean X-ray and neutron SLD profiles as a function of the film depth z can be respectively expressed as:

$$\rho_X(z) = f_{v1}(z)\rho_{X1} + f_{v2}(z)\rho_{X2} \quad (1)$$

and

$$\rho_N(z) = f_{v1}(z)\rho_{N1} + f_{v2}(z)\rho_{N2} \quad (2)$$

in terms of the PCBM and P3HT volume fraction profiles, $f_{v1}(z)$ and $f_{v2}(z)$, averaged over the plane at the film depth z. Based on the mean densities, 1.10 ± 0.02 and 1.50 ± 0.05 g cm^{-3}, determined respectively for pure P3HT and PCBM films, using X-ray reflectivity (Fig. S1 in the ESI†), the X-ray and neutron SLD values ρ_{x1} and ρ_{N1} for pure PCBM are 12.9 and 4.34×10^{-6} $Å^{-2}$, respectively, whereas ρ_{x2} and ρ_{N2} for pristine P3HT are 10.2×10^{-6} and 0.676×10^{-6} $Å^{-2}$. The densities of pure PCBM and

P3HT films are consistent with those used previously.[17] Because of the larger neutron scattering contrast ($\rho_{N1} - \rho_{N2}$) between PCBM and P3HT than the X-ray one ($\rho_{x1} - \rho_{x2}$), neutrons are relatively more sensitive to PCBM distribution but insensitive to P3HT; whereas X-rays are sensitive to either component (though with a lower distinguishing power) due to the high X-ray SLD values. We found that the commonly used two-phase assumption, $f_{v1} + f_{v2} = 1.0$, would lead to unreasonable negative f_{v2} values for P3HT, when both the fitted neutron and X-ray SLD values are taken into account in eqn (1) and (2). Consequently, we have to use porosity with a volume fraction f_{v3} as the third component for the redefined volume fraction conservation $f_{v1} + f_{v2} + f_{v3} = 1.0$, then solve for f_{v1} and f_{v2} jointly based on the contrast neutron and X-ray SLD values obtained for the sample. Rearranging eqn. (1) and (2) leads to

$$f_{v1}(z) = [-\rho_{N2}\rho_X(z) + \rho_{X2}\rho_N(z)]/\Delta \quad (3)$$

and

$$f_{v2}(z) = [\rho_{N1}\rho_X(z) - \rho_{X1}\rho_N(z)]/\Delta, \quad (4)$$

with $\Delta = \rho_{N1}\rho_{X2} - \rho_{X1}\rho_{N2}$. Then, the porosity can be obtained from the unity conservation of the volume fractions.

3. Results and discussion

X-Ray and neutron SLD profiles

Shown in Fig. 1a are the XR data measured for the annealed P3HT/PCBM ($c = 0.8$) film. The data exhibit fine Kiessig fringes up to the high q_z-region (>0.25 Å^{-1}), reflecting the highly stratified morphology of a film thickness of ~85 nm (estimated from the frequency of the fringes). Using the SLD profile $\rho_X(z)$ shown in the inset of Fig. 1a, we could fit nearly perfectly the data. The best-fitted SLD profile comprises a surface layer (~10 nm, not including the surface roughness ~5 nm) of a significantly lower ρ_X value followed by a main layer (~70 nm) of uniform ρ_X on top of that for the Si-substrate. The corresponding NR data measured for the same film are shown in Fig. 1b. With the same fitting algorithm as that used for the XR data, the NR data were fitted decently using a three-layer model of neutron SLD $\rho_N(z)$ (inset of Fig. 1b), in contrast to the two-layer model used in the XR data fitting. The three-layer model consists of a surface layer of ~10 nm (not including the ~5 nm surface roughness), a uniform main layer of ~50 nm, and a characteristic interfacial layer (~20 nm) of a high SLD peak contributed presumably by the enriched PCBM.[16,17] Note that PCBM has a much higher ρ_N value than that of P3HT; hence, the fitted neutron SLD profile reflects essentially the vertical distribution of PCBM across the film. As shown in the insets of Fig. 1a and b, the characteristically different features in the contrast neutron and X-ray SLD profiles near the film surface and interface imply the existence of the third phase, presumably porosity, in these interfacial zones, as detailed below.

Vertical composition profile

Shown in Fig. 2a are the in-depth volume fraction profiles of the PCBM, P3HT, and porosity deduced from the two contrast SLD

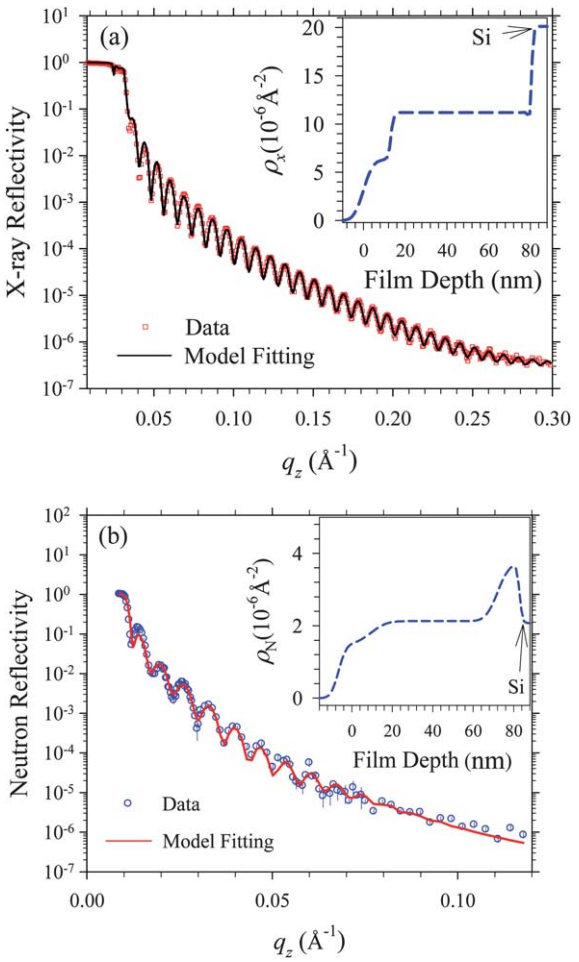

Fig. 1 XR (a) and NR (b) data for the same annealed P3HT/PCBM ($c = 0.8$) film on Si wafer. The two sets of data are respectively fitted (solid curves) using the SLD profiles shown in the insets.

profiles of X-ray and neutrons (insets of Fig. 1a and b) for the annealed P3HT/PCBM film, based on eqn (3) and (4). The deduced distribution of PCBM along the film in-depth direction is characterized by the gradually increased PCBM concentration in the thin surface layer in conjunction with the constant PCBM volume fraction of $f_v \approx 40\%$ of the main layer; PCBM furthermore enriches in the interface layer to a peak value of $f_v \approx 80\%$. In contrast, the deduced vertical distribution of P3HT (Fig. 2) manifests a low concentration near the surface ($f_v \approx 20\%$), which transits abruptly to the relatively high and constant P3HT volume fraction $f_v \approx 60\%$ of the main layer, then gradually depletes in the interface layer. The most striking features revealed by these deduced volume fraction profiles in Fig. 2 are porosity values of *ca.* 40% and 15% in the surface and interface layers, respectively, as highlighted in the shaded areas in Fig. 2a. In contrast, the main layer exhibits a solid structure (without discernible porosity) of a constant P3HT/PCBM composition. Note that in the surface layer the *absolute* volume fractions of PCBM and P3HT are *ca.* 30% and 20%, respectively. Because of this, tools of selective sensitivity to merely PCBM or P3HT might have alluded to a surface enrichment of the other component that is insensitive to the tools, provided the two-phase assumption is used without calibration to absolute volume fractions.

This journal is © The Royal Society of Chemistry 2011

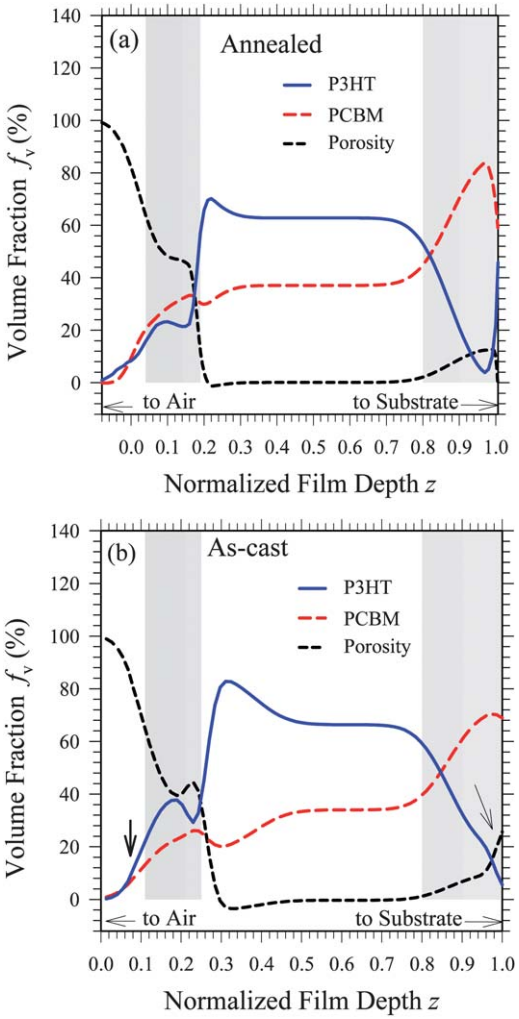

Fig. 2 Vertical volume fraction profiles of the PCBM, P3HT, and porosity for the 150 °C annealed (a) and the as-cast (b) P3HT/PCBM films (with the film thickness normalized by 85 nm). Shaded areas of nontrivial f_v values are the surface and interface layers, respectively. The sharper, unnatural transitions of the f_v profiles at $z \sim 0.24$ and ~ 0.98 in (b) are resulted from the fine structural features of a few nanometres resolved by the XR data but not by the NR data of a limited q_z-range, hence a lower resolution of a few nanometres (*cf.* Fig. S2 and S3 in the ESI†).

We have also attempted to deduce the in-depth composition profile using residual solvent (CB) as the third phase. The substantial density of CB (1.11 g cm^{-3}), hence SLD values, however, led to an unphysically negative volume fraction of P3HT in the surface layer. In practice, it would be difficult to have a substantial volume fraction of residual CB at the film surface after 15 min annealing at 150 °C (above the boiling point 131 °C of CB). We have thus excluded the possibility of using residual solvent as the third phase.

To better address the mechanism of the vertical (*i.e.* along the film in-depth direction) phase separation behavior observed for the P3HT/PCBM blend, especially the formation of a porous surface layer, we first separate the annealing effects from that induced by the spin-casting process (or solvent evaporation) on the vertical phase separation. We show in Fig. 2b the similarly extracted volume fraction profiles of P3HT, PCBM, and the porosity for the as-cast film (*cf.* data-fitting results in Fig. S2 and S3 of the ESI†). Comparison of these f_v profiles of the as-cast film and that of the annealed film (Fig. 2a and b) leads to the following conclusions: (i) similar surface and interface porosities already existed in the as-cast film, and were modestly smoothed (especially near the interface adjacent to the Si substrate) but not eliminated upon 150 °C annealing; (ii) annealing promoted vertical diffusions of P3HT and PCBM, leading to more uniformly distributed P3HT and PCBM in the surface and the main layers; (iii) the PCBM concentration peaked at ~5 nm from the interface which dropped quickly to $f_v \approx 50\%$ near the interface. We note that the roughly balanced PCBM and P3HT volume fractions at the interface (despite the overall enrichment of PCBM in the interfacial zone) and especially the high surface porosity (with a low P3HT volume fraction of ~20%) may discount somewhat the advantage of utilizing the vertical phase separation features for the inverted structure solar cells proposed.[14,26,27] On the other hand, the promoted vertical diffusions of P3HT and PCBM upon annealing are in accord with previous results.[8,16–18,21,28–31] In general, annealing facilitates either vertical inter-diffusion or phase separation of the two components, depending on the initial composition/phase separation of the film or the P3HT–PCBM miscibility phase diagram.[31] Fig. 3 shows a typical AFM image of the annealed P3HT–PCBM film ($c = 0.8$); the scattered dark spots (*ca.* zero reference height) among highlands presumably contribute to the surface porosity revealed from the NR/XR results.

Local phase separation

Using the NSRRC BL23A GISAXS/GIWAXS instrument,[12,32] we furthermore observed that 150 °C annealing could significantly enhance the GISAXS intensity (Fig. 4) and P3HT lamellar peak intensity (Fig. S4 in the ESI†) of a similar P3HT/PCBM film, implying significantly increased local phase separation for PCBM aggregation and P3HT crystallization, hence the device performance (*cf.* Fig. S5 in the ESI†). GISAXS data fitting, on

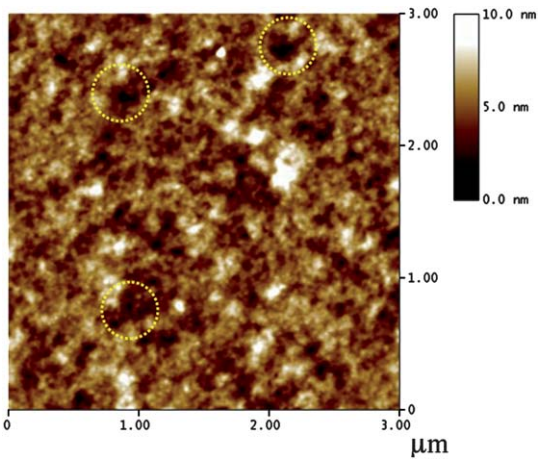

Fig. 3 AFM image of the 150 °C annealed P3HT–PCBM film ($c = 0.8$). The scale bar covers 10 nm surface height variations. The scattered dark zones (selectively circled) are of ~zero reference height.

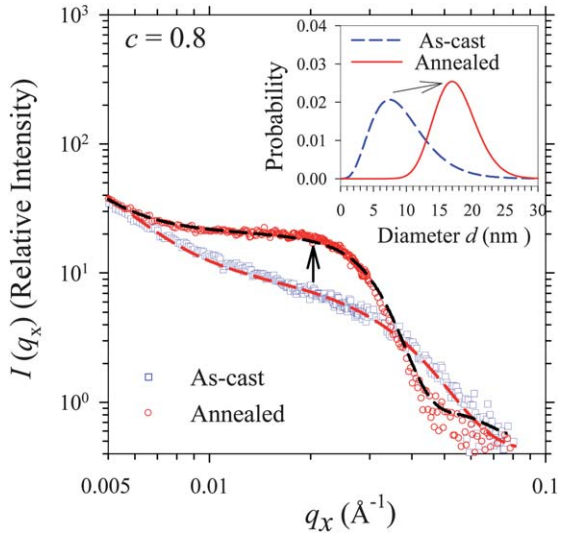

Fig. 4 GISAXS profiles along the film in-plane direction (q_x) for a P3HT/PCBM film, with $c = 0.8$, before and after 150 °C annealing. The data are respectively fitted (dashed curves) using polydisperse spheres with the Schultz size distributions shown in the inset.

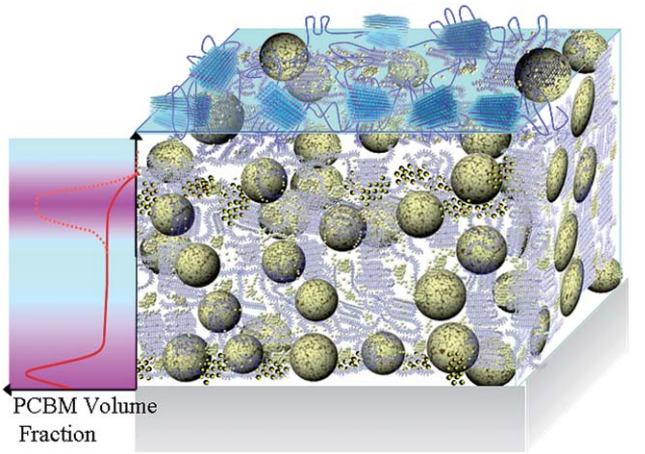

Fig. 5 Cartoon for an optimized morphology of P3HT/PCBM thin film solar cells. Intercalated PCBM aggregates (large spheres) and P3HT lamellar domains (work-like stacks) are dispersed in the matrix of amorphous chains of P3HT with dissolved PCBM (small spheres). To the left: vertical P3HT- and PCBM-enriched regions are colored sky blue and pink, respectively, together with the PCBM volume fraction profile (solid curve). The dotted curve near the surface depicts an additional PCBM-enriched layer accumulated below the surface P3HT layer, when the PCBM concentration of the film exceeds the miscibility limit of $c \gtrsim 1.0$ (*cf.* Fig. 6b below).

the basis of a model of polydisperse spheres (detailed in the ESI†), reveals that PCBM aggregated drastically from a diameter of $d \approx 7$ nm (with polydispersity $p = 45\%$) to ~18 nm ($p = 15\%$) upon annealing, as illustrated in the inset of Fig. 4. In the GISAXS data fitting, a hard-sphere structure factor was also included to characterize the loose ordering of the PCBM aggregates revealed by the shoulder peak at the in-plane scattering wavevector $q_x \approx 0.02$ Å^{-1} (Fig. 4);[33] the thus fitted mean PCBM aggregate spacing is 26 nm with an aggregation volume fraction of 18% (*cf.* ESI†). Considering the 37% prescribed PCBM volume fraction, the result implies a significant amount (19%) of non-aggregate PCBM dispersed in the P3HT matrix, which is consistent with the ~20 wt% molecular solubility of PCBM in P3HT proposed previously.[28,30,31]

Compared to the vertical (1D) phase separation revealed from NR/XR for the stratified structure that would occur upon film drying, the local phase separation for the growth of (3D) PCBM aggregates and perfection of P3HT lamellae obviously required annealing to activate, thus of a different origin. By integrating the XR/NR and GISAXS/GIWAXS results, we would suggest that the modest changes in the vertical phase separation upon annealing were resulted from diffusions or transportations of non-aggregated PCBM molecules and amorphous P3HT chains; while part of the demixed PCBM and P3HT formed intercalated nanodomains, hence were localized in the main layer within the metastable regime, $c \lesssim 1.0$ and $T < 200$ °C, of the blend.[31] Nevertheless, the local density inhomogeneity owing to the intercalated, heterogeneous nanodomains could be smeared out after in-plane averaging, leading to the uniform $f_v(z)$ of the main layer illustrated in Fig. 2a. Fig. 5 illustrates an optimized morphology of the annealed P3HT/PCBM film on the basis of the vertical phase separation features observed with NR/XR and the local phase separation for PCBM and P3HT nanodomains observed with GISAXS/GIWAXS.

Composition dependence

We have made further XR and NR measurements for the P3HT/PCBM films with different compositions of $c = 0.6$ and 1.0. The similarly extracted volume fraction profiles (Fig. 6), from the best-fitted SLD profiles (Fig. S6–S9 in the ESI†), share resembling porosity features as those described above for the blend film with $c = 0.8$, specifically the ~10 nm surface layer of *ca.* 40% porosity and the 15 nm PCBM-enriched interface layer of ~15% porosity. Note that for the $c = 1.0$ case, a significant amount of demixed PCBM started to accumulate below the surface P3HT layer (Fig. 6b), as the metastable phase boundary ($c \lesssim 1.0$) of the PCBM/P3HT blend was approached in this case;[31] and the annealing could effectively enhance the excess PCBM to phase-separate out from the main layer (*cf.* the PCBM composition profile for the as-cast film shown in Fig. S9†). Nevertheless, in view of all the results, porous features near the film surface and film/substrate interface of the P3HT/PCBM blend appear to be common in the composition range ($c = 0.6$–1.0) and temperature (as-cast and 150 °C annealed) studied.

Phase separation mechanism

Holes and islands (of various shapes) are frequently seen on the surfaces of spun-cast conjugate polymer thin films featuring oriented lamellar domains, as a consequence of surface energy minimization.[34–36] By controlling interface tensions *via* mixing solvents and solvent evaporation rate, pores of spun-cast polymer films could be manipulated to be enriched near the surface or away from the surface and into the bulk.[35] Pore formation at the surface of the P3HT/PCBM blend observed here obviously involves more interacting kinetics and thermodynamic parameters of demixing (miscibility), solvent evaporation, polymer

This journal is © The Royal Society of Chemistry 2011

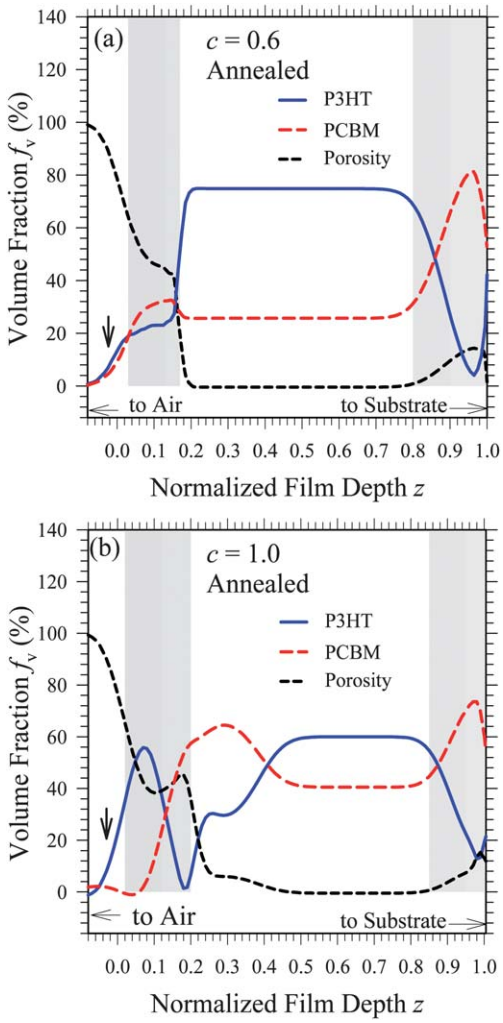

Fig. 6 Vertical volume fraction profiles of the PCBM, P3HT, and porosity of the 150 °C annealed P3HT/PCBM films with $c = 0.6$ (a) and 1.0 (b) (film thickness normalized by 85 nm). The profiles are deduced from the corresponding sets of contrast NR/XR SLD profiles (Fig. S6 and S9 in the ESI†). Shaded areas highlight the surface and interface zones containing porosity. The arrows mark the air–film transition (roughness) zones.

crystallization, fullerene aggregation, and thermal fluctuations in terms of surface capillary waves.[8,20,21,36] As the surface pore features of the P3HT/PCBM films were considerably stable to the applied annealing, thermodynamic parameters likely dominated (though not completely) the final surface pore morphology of the films. In contrast, the porosity (~30%) near the Si interface of the as-cast film could be removed substantially after annealing (Fig. 2a and b), and therefore should be substantially dependent on the kinetic parameters.

The formation mechanism of thermally stable surface pores may be understood better in terms of the phase diagram of the P3HT/PCBM blend. In this regard, previously reported phase diagrams[28,31] of P3HT/PCBM indicated that below ~200 °C and within the composition of $c = 0.5$–1.0 (the most-often studied composition range for this efficient suite of BHJ solar cells), the PCBM/P3HT blend could form a metastable phase, owing largely to the miscibility between P3HT and PCBM.[31] A consequence is that even we can quench quickly enough the spun-cast film from a homogeneous mixture for phase separation (*via* fast solvent evaporation or spin-casting speed), spinodal decomposition for a bicontinuous phase may not likely take place in this metastable region. A more favored process may be a relatively slower phase separation of P3HT and PCBM *via* nucleation-and-growth in minimizing the surface/free energy of the system,[12] as also proposed recently based on *in situ* GIWAXS for the film drying process;[37] the dominating thermodynamic parameters thus include surface tensions and the interaction parameters among the three components of polymer, fullerene-derivative, and solvent. We notice that the surface tension of 33 mN m^{-1} of the solvent chlorobenzene used in the film casting is in-between that of P3HT (27 mN m^{-1}) and PCBM (38 mN m^{-1}).[14] It may be that during the last stage of the film thinning/drying process, concentration fluctuations amplified upon the increasing higher polymer/fullerene derivative concentrations finally break the very thin transient surface layer[36,37] into some sort of an *inverse-micelle(worm)-like structure* with residual solvent trapped inside (for a lower free energy state). Evaporation of the solvent leads to a porous surface layer with the often observed P3HT fibril-mesh structure,[19,38] in which PCBM (awaiting demixing/aggregation upon annealing) resides either underneath or in-between the P3HT fibrils for minimizing the surface energy. Adjusting the solvent, the polymer/fullerene-derivative composition, and the interaction parameters among the three components, may manipulate the phase separation behavior of the blend,[39,40] likewise the porosity features. Efforts along this direction have been taken in search of efficient routes for controlling the interfacial morphology and vertical phase separation of the blends *via* selectively modified conjugate polymers and/or fullerene derivatives for modulating the surface energy or miscibility of the two components.[14,27,41,42]

4. Conclusions

Using contrast variation of X-ray and neutron reflectivity with a high spatial resolution in the film in-depth direction and a three-phase model, we have revealed the vertical phase separation behavior of the composite film of P3HT/PCBM. The stratified composition profiles obtained for the films comprise, in general, a porous surface layer, a solid main layer, and a PCBM-enriched interface layer of small porosity; a PCBM-excess-layer starts to form beneath the surface P3HT layer when the metastable miscibility limit of the two components is approached (~1 : 1 weight ratio). Within the composition range and the annealing temperature studied, annealing influences modestly the global vertical (1D) phase separation of the film *via* diffusions of non-localized PCBM molecules and P3HT amorphous chains. In contrast, a substantial amount of demixed PCBM and P3HT upon annealing formed intercalated, hence localized, PCBM and P3HT nanograins, as revealed by GISAXS/GIWAXS; such critical local phase separation for significantly improved device performance contributes, however, marginally to the global changes in the vertical composition profile. The observed high surface porosity and the concentration-dependent vertical volume fractions of P3HT and PCBM not only help to reconcile several previously seemingly opposite conclusions reported on the surface composition of the BHJ thin-film solar cells, but also

provide hints on the mechanistic origins of the related phase separation behavior.

Acknowledgements

Discussion with Prof. T.-S. Huang is acknowledged. We thank Dr H.-Y. Lee for the access of the X-ray reflectometer, and Mr M.-S. Su for sample preparation. Neutron reflectivity measurement was performed in the S-type research project of High Energy Accelerator Research Organization (2009S08).

References

1 X. Yang and J. Loos, *Macromolecules*, 2007, **40**, 1353.
2 J. M. Frost, F. Cheynis, S. M. Tuladhar and J. Nelson, *Nano Lett.*, 2006, **6**, 1674.
3 J. S. Moon, J. K. Lee, S. Cho, J. Byun and A. J. Heeger, *Nano Lett.*, 2009, **9**, 230.
4 C. Muller, T. A. M. Ferenczi, M. Campoy-Quiles, J. M. Frost, D. D. C. Bradley, P. Smith, N. Stingelin-Stutzmann and J. Nelson, *Adv. Mater.*, 2008, **20**, 3510.
5 Y. Kim, S. Cook, S. M. Tuladhar, S. A. Choulis, J. Nelson, J. R. Durrant, D. D. C. Bradley, M. Giles, I. McCulloch, C. S. Ha and M. Ree, *Nat. Mater.*, 2006, **5**, 197.
6 M. Shin, H. Kim, J. Park, S. Nam, K. Heo, M. Ree, C.-S. Ha and Y. Kim, *Adv. Funct. Mater.*, 2010, **20**, 748.
7 E. Verploegen, R. Mondal, C. J. Bettinger, S. Sok, M. F. Toney and Z. Bao, *Adv. Funct. Mater.*, 2010, **20**, 3519.
8 D. Chen, A. Nakahara, D. Wei, D. Nordlund and T. P. Russell, *Nano Lett.*, 2011, **11**, 561.
9 J. W. Kiel, A. P. R. Eberle and M. E. Mackay, *Phys. Rev. Lett.*, 2010, **105**, 168701.
10 M. Y. Chiu, U. Jeng, M. S. Su and K. H. Wei, *Macromolecules*, 2010, **43**, 428.
11 M. Y. Chiu, U. Jeng, C. H. Su, K. S. Liang and K. H. Wei, *Adv. Mater.*, 2008, **20**, 2573.
12 W. R. Wu, U. Jeng, C. J. Su, K. H. Wei, M. S. Su, M. Y. Chiu, C. Y. Chen, W. B. Wu, C. H. Su and A. C. Su, *ACS Nano*, 2011, DOI: 10.1021/nn2010816.
13 W. Ma, C. Yang, X. Gong, K. Lee and A. J. Heeger, *Adv. Funct. Mater.*, 2005, **15**, 1617.
14 L. M. Chen, Z. Xu, Z. Hong and Y. Yang, *J. Mater. Chem.*, 2010, **20**, 2575.
15 Z. Xu, L. M. Chen, G. Yang, C. H. Huang, J. Hou, Y. Wu, G. Li, C. S. Hsu and Y. Yang, *Adv. Funct. Mater.*, 2009, **19**, 1227.
16 J. W. Kiel, B. J. Kirby, C. F. Majkrzak, B. B. Maranville and M. E. Mackay, *Soft Matter*, 2010, **6**, 641.
17 A. J. Parnell, A. D. F. Dunbar, A. J. Pearson, P. A. Staniec, A. J. C. Dennison, H. Hamamatsu, M. W. A. Skoda, D. G. Lidzey and R. A. L. Jones, *Adv. Mater.*, 2010, **22**, 2444.
18 M. Campoy-Quiles, T. Ferenczi, T. Agostinelli, P. G. Etchegoin, Y. Kim, T. D. Anthopoulos, P. N. Stavrinou, D. D. C. Bradley and J. Nelson, *Nat. Mater.*, 2008, **7**, 158.
19 S. S. van Bavel, E. Sourty, G. de With and J. Loos, *Nano Lett.*, 2009, **9**, 507.
20 Y. Vaynzof, D. Kabra, L. Zhao, L. L. Chua, U. Steiner and R. H. Friend, *ACS Nano*, 2011, **5**, 329.
21 D. Chen, F. Liu, C. Wang, A. Nakahara and T. P. Russell, *Nano Lett.*, 2011, **11**, 2071.
22 Y. S. Huang, U. Jeng, C. H. Hsu, N. Torikai, H. Y. Lee, K. Shin and M. Hino, *Phys. B*, 2006, **385–386**, 667.
23 C. H. Hsu, U. Jeng, H. Y. Lee, C. M. Haung, K. S. Liang, D. Windover, T. M. Lu and C. Jin, *Thin Solid Films*, 2004, **472**, 323.
24 K. Mitamura, N. L. Yamada, H. Sagehashi, H. Seto, N. Torikai, T. Sugita, M. Furusaka and A. Takahara, *J. Phys.: Conf. Ser.*, 2011, **272**, 012017.
25 http://parratt32.software.informer.com/.
26 N. D. Treat, M. A. Brady, G. Smith, M. F. Toney, E. J. Kramer, C. J. Hawker and M. L. Chabinyc, *Adv. Energy Mater.*, 2011, **1**, 82.
27 D. S. Germack, C. K. Chan, R. J. Kline, D. A. Fischer, D. J. Gundlach, M. F. Toney, L. J. Richter and D. M. DeLongchamp, *Macromolecules*, 2010, **43**, 3828.
28 B. A. Collins, E. Gann, L. Guignard, X. He, C. R. McNeill and H. Ade, *J. Phys. Chem. Lett.*, 2010, **1**, 3160.
29 J. S. Moon, C. J. Takacs, Y. Sun and A. J. Heeger, *Nano Lett.*, 2011, **11**, 1036.
30 P. E. Hopkinson, P. A. Staniec, A. J. Pearson, A. D. F. Dunbar, T. Wang, A. J. Ryan, R. A. L. Jones, D. G. Lidzey and A. M. Donald, *Macromolecules*, 2011, **44**, 2908.
31 J. Y. Kim and C. D. Frisbie, *J. Phys. Chem. C*, 2008, **112**, 17726.
32 U. Jeng, C. H Su, C. J. Su, K. F. Liao, W. T. Chuang, Y. H. Lai, J. W. Chang, Y. J. Chen, Y. S. Huang, M. T. Lee, K. L. Yu, J. M. Lin, D. G. Liu, C. F. Chang, C. Y. Liu, C. H. Chang and K. S. Liang, *J. Appl. Crystallogr.*, 2010, **43**, 110.
33 S. H. Chen, E. Y. Sheu, J. Kalus and H. Hoffmann, *J. Appl. Crystallogr.*, 1988, **21**, 751.
34 R. J. Kline, M. D. McGehee, E. N. Kadnikova, J. Liu, J. M. J. Fréchet and M. F. Toney, *Macromolecules*, 2005, **38**, 3312.
35 M. S. Park, W. Joo and J. K. Kim, *Langmuir*, 2006, **22**, 4594.
36 S. Y. Heriot and R. A. L. Jones, *Nat. Mater.*, 2005, **4**, 782.
37 T. Wang, A. D. F. Dunbar, P. A. Staniec, A. J. Pearson, P. E. Hopkinson, J. E. MacDonald, S. Lilliu, C. Pizzey, N. J. Terrill, A. M. Donald, A. J. Ryan, R. A. L. Jones and D. G. Lidzey, *Soft Matter*, 2010, **6**, 4128.
38 C. Y. Chen, S. H. Chan, J. Y. Li, K. H. Wu, H. L. Chen, J. H. Chen, W. Y. Huang and S. A. Chen, *Macromolecules*, 2010, **43**, 7305.
39 S. Nilsson, A. Bernasik, A. Budkowski and E. Moons, *Macromolecules*, 2007, **40**, 8291.
40 A. S. Anselmo, L. Lindgren, J. Rysz, A. Bernasik, A. Budkowski, M. R. Andersson, K. Svensson, J. van Stam and E. Moons, *Chem. Mater.*, 2011, **23**, 2295.
41 M. A. Ruderer and P. Müller-Buschbaum, *Soft Matter*, 2011, **7**, 5482.
42 J. S. Kim, Y. Lee, J. H. Lee, J. H. Park, J. K. Kim and K. Cho, *Adv. Mater.*, 2010, **22**, 1355.

 This journal is © The Royal Society of Chemistry 2011